ČESKÉ VYSOKÉ
UČENÍ TECHNICKÉ
V PRAZE

FAKULTA JADERNÁ
A FYZIKÁLNĚ
INŽENÝRSKÁ

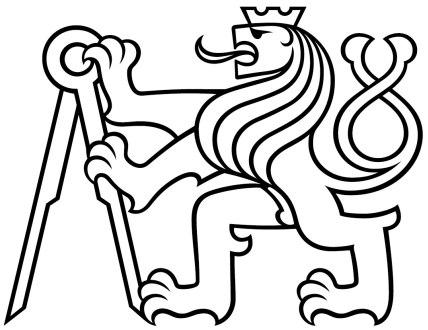

VÝZKUMNÝ ÚKOL

2023

FILIP
KOŇAŘÍK

ČESKÉ VYSOKÉ UČENÍ TECHNICKÉ V PRAZE

FAKULTA JADERNÁ A FYZIKÁLNĚ INŽENÝRSKÁ

Porovnání simulací energetické kalibrace SuperNEMO demonstrátoru s prvními naměřenými daty

Výzkumný úkol

Autor práce: Bc. Filip Koňařík
Vedoucí práce: Mgr. Miroslav Macko, Ph.D.
Konzultant: Ing. Dominika Mašlárová
Školní rok: 2022/2023

Před svázáním místo této stránky vložíte zadání práce s podpisem děkana (v jedné kopii práce bude list s originálem podpisu). Toto bude jediný oboustranný list ve Vaší práci!

Thesis title:
Comparison of the energy calibration simulations of the SuperNEMO Demonstrator with the first measured data

Author: Bc. Filip Koňařík

Specialization: Computational physics

Thesis type: Research project

Supervisor: Mgr. Miroslav Macko, Ph.D.

Consultant: Ing. Dominika Mašlárová

Abstract: SuperNEMO is an experiment designed to search for neutrinoless double beta decay. Energy measurement of electrons from the decay is performed using segmented calorimeter consisting of 712 optical modules. To keep sufficient energy resolution it is necessary to periodically calibrate all optical modules. SuperNEMO has recently started to take its first calibration data. The thesis is focused on comparison between previous Monte Carlo simulations and new calibration data. First of all, three event selection algorithms were tested and compared. The most precise one has been chosen for further data processing. Exposures of optical modules has been extracted from the calibration data and compared with values from simulations. The shape of energy spectra measured by optical modules has also been investigated. The final part of the thesis discusses the problem of calibration electrons losing part of its energy. This effect can significantly influence precision of the calibration. To compensate for it a correction has been developed in the past. The thesis proposes potential improvements of the correction.

Key words: double beta decay, SuperNEMO, neutrino, energy calibration

Contents

Introduction **6**

1 Neutrino physics and SuperNEMO experiment **7**
1.1 Neutrino . . . 7
1.2 Double beta decay . . . 9
1.2.1 Two-neutrino double beta decay ($2\nu\beta\beta$) . . . 9
1.2.2 Neutrinoless double beta decay ($0\nu\beta\beta$) . . . 9
1.3 Homogeneous detectors . . . 11
1.4 SuperNEMO experiment . . . 11
1.4.1 Main detector systems . . . 12
1.4.2 Calorimeter calibration . . . 14

2 Calibration data analysis **17**
2.1 Simulated data . . . 17
2.2 Real data . . . 18
2.2.1 Tracker signal . . . 18
2.2.2 Calorimeter signal . . . 19
2.2.3 SuperNEMO data formats . . . 21
2.3 Calibration data and event selection . . . 22
2.3.1 Event . . . 22
2.3.2 Event selection . . . 22
2.3.3 Comparison of simulation with real data . . . 24
2.3.4 Calibration spectrum corrections . . . 27

Summary **33**

Introduction

Standard Model is the most general theory of elementary particles and fundamental forces which we have today. However, it is already clear that there are questions which it cannot answer. One famous example is the dark matter. It is known to attract astronomical objects through gravitational interaction, but its structure on level of elementary particles is still unknown. Such problems lead us to conclusion that further development of particle physics will require us to study physics beyond the Standard Model.

One possible way to search for physics beyond the Standard Model is through properties of neutrinos. Neutrinos are leptons abundant in the whole universe which very rarely interact with matter. There are three masses and three flavours of neutrinos. Very important was the discovery of neutrino oscillations. Thanks to this phenomenon neutrinos change their flavour while traveling through space. Direct implication of this fact is that the mass of neutrino is non-zero. This goes against the Standard Model which considers neutrinos to be massless. That is why neutrinos could potentially be a suitable tool to discover new physics.

Measurements of neutrino oscillations can provide information about differences between the three neutrino masses. This way, however, absolute values of these masses cannot be measured. One possible way to measure them is through measurement of half-life of neutrinoless double beta decay ($0\nu\beta\beta$) which is in direct relationship with neutrino masses. $0\nu\beta\beta$-decay is, however, yet to be observed and its existence is uncertain. To this day, experiments have only been able to set the lower limit of its half-life.

One of the experiments searching for $0\nu\beta\beta$-decay is SuperNEMO. Its so-called tracko-calo design is unique in the field. It has ability to measure both trajectories and energies of electrons from $0\nu\beta\beta$-decay contrary to other experiments which usually only measure the energies. To measure energies, it uses calorimeter consisting of 712 so-called Optical Modules (OMs) composed of a plastic scintillator coupled with photomultiplier tube (PMT). To keep sufficient energy resolution, it is important to periodically perform energy calibration of all OMs. For this purpose an automatic calibration system has been created. It consists of 42 ^{207}Bi calibration sources which can be inserted inside the detector using 6 stepper motors.

Last year, SuperNEMO started taking first calibration data. The main goal of this thesis is to compare previous analysis performed on simulated data with the newly obtained real data. The first chapter very briefly introduces neutrino physics, different experiments searching for $0\nu\beta\beta$-decay and the SuperNEMO experiment. The second chapter is focused on processing of real data and its comparison with simulations.

Chapter 1

Neutrino physics and SuperNEMO experiment

1.1 Neutrino

Neutrino is an elementary particle well-known for its very rare interaction with matter. It is a lepton with zero charge which mostly interacts through Weak interaction. Due to this it is very hard to detect. Currently we distinguish three flavours of neutrinos - electron (e), muon (μ) and tau (τ) neutrino, as well as three masses m_1, m_2 and m_3. These flavours and masses have their corresponding eigenstates. Their relationship is given by so-called Pontecorvo–Maki–Nakagawa–Sakata (PMNS) matrix.

$$\begin{pmatrix} |\nu_e\rangle \\ |\nu_\mu\rangle \\ |\nu_\tau\rangle \end{pmatrix} = \begin{pmatrix} U_{e1} & U_{e2} & U_{e3} \\ U_{\mu 1} & U_{\mu 2} & U_{\mu 3} \\ U_{\tau 1} & U_{\tau 2} & U_{\tau 3} \end{pmatrix} \begin{pmatrix} |\nu_1\rangle \\ |\nu_2\rangle \\ |\nu_3\rangle \end{pmatrix} \tag{1.1}$$

Here $|\nu_e\rangle$, $|\nu_\mu\rangle$ and $|\nu_\tau\rangle$ are electron, muon and tau eigenstates, $|\nu_1\rangle$, $|\nu_2\rangle$ and $|\nu_3\rangle$ are mass eigenstates and $U_{\alpha i}$ are PMNS matrix elements. In the Standard Model (SM) neutrinos are described as massless. This has been, however, refuted by discovery of neutrino oscillations [1]. This phenomenon causes neutrinos to change their flavour while they pass through space. The neutrino which was emitted with electron flavour can be later observed as muon or tau neutrino. Without loss of generality, we can consider only two flavours (α and β) and require PMNS matrix elements to be real numbers. The equation (1.1) can be then written as:

$$\begin{pmatrix} |\nu_\alpha\rangle \\ |\nu_\beta\rangle \end{pmatrix} = \begin{pmatrix} \cos(\theta) & \sin(\theta) \\ -\sin(\theta) & \cos(\theta) \end{pmatrix} \begin{pmatrix} |\nu_1\rangle \\ |\nu_2\rangle \end{pmatrix}, \tag{1.2}$$

where the relationship between eigenstates is now given only by so-called mixing angle θ. The probability of transition from eigenstate α to β can then be calculated using following formula [2]

$$P\left(\nu_\alpha \to \nu_\beta\right) = \sin^2(2\theta)\sin^2\left(\frac{\Delta m_{ij}^2 L}{4E}\right), \tag{1.3}$$

where E is neutrinos energy, L is the distance it has traveled and $\Delta m_{ij}^2 = m_i^2 - m_j^2$ is the difference of squared eigenmasses of i-th and j-th state. For the probability to be non-zero at least one of the eigenmasses is required to be non-zero.

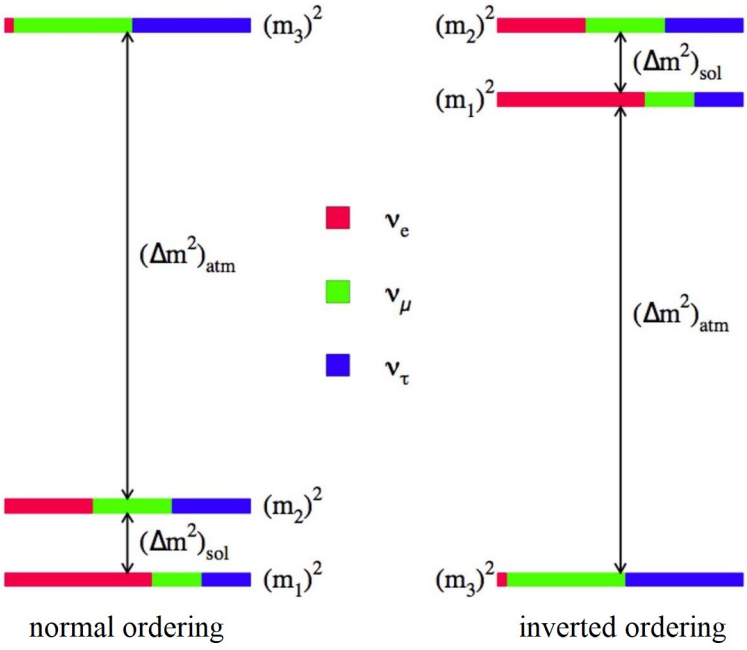

Figure 1.1: Two possible orderings of neutrino masses are currently considered - normal ordering and inverted ordering. In the picture we can see their comparison. Coloured bars represent mass eigenstates as superpositions of flavour eigenstates. The figure was adapted from Cahn et al [3].

Even though, we know that the neutrino mass is not zero, its absolute value is yet to be measured. Current experiments are only able to measure differences Δm_{ij} through observation of neutrino oscillations. The masses themselves, however, cannot be determined in the same way. Without knowing the absolute values of masses we also cannot determine their ordering. This ambiguity is represented in the figure 1.1. As electron is the lightest particle out of electron, muon, tauon triplet it is intuitively expected that the mass eigenstate with the highest abundance of electron flavour would be the lightest one. This is called "normal ordering". The second option is so-called "inverted ordering" where the eigenstate with lowest electron flavour abundance is the lightest one.

There are three main approaches of neutrino mass measurement. The first one is based on very precise measurement of beta decay electron spectrum where the mass is then determined from the position and the shape of the end of the spectrum (KATRIN experiment [4]). The second approach is based on cosmological models. Neutrinos play important role in formation of cosmological structures. Thanks to that, it is possible to estimate the sum of mass eigenvalues $\sum m_i$ based on astronomical observations (Planck collaboration [5]). The last approach of mass measurement is based on neutrinoless double beta decay and will be described in the following section using similar explanation as in our previous work [6](in Czech).

1.2 Double beta decay

1.2.1 Two-neutrino double beta decay ($2\nu\beta\beta$)

Two-Neutrino Double Beta Decay is a type of radioactive decay predicted by Maria Goeppert-Mayer in 1935. In $2\nu\beta\beta$ two neutrons in the atomic nucleus are transformed into two protons followed by emission of two electrons and two antineutrinos [7]:

$$(A, Z) \rightarrow (A, Z + 2) + 2e^{-} + 2\bar{v}_e. \tag{1.4}$$

For the decay to occur, its Q-value defined as a difference between nucleus mass after and before the decay has to be positive. The mass of the nucleus can be written as

$$m(Z, N) = Zm_p + Nm_n - E_B(Z, N), \tag{1.5}$$

where $m(Z, N)$ is the mass of nucleus with Z protons and N neutrons, m_p and m_n are rest masses of proton and neutron and $E_B(Z, N)$ is binding energy of the nucleus. We can express the binding energy using Weizsäcker equation

$$E_B = a_V A - a_S A^{2/3} - a_C \frac{Z(Z-1)}{A^{1/3}} - a_A \frac{(N-Z)^2}{A} + \delta(N, Z), \tag{1.6}$$

where A is a mass number and a_V, a_S, a_C, a_A and $\delta(N, Z)$ are measured constants belonging to volume term, surface term, Coulomb term, asymmetry term and pairing term, respectively. The pairing term can take on three different values

$$\delta(N, Z) = \begin{cases} \frac{a_p}{\sqrt{A}} & Z, N \text{ even } (A \text{ even}), \\ 0 & A \text{ odd}, \\ -\frac{a_p}{\sqrt{A}} & Z, N \text{ odd } (A \text{ even}). \end{cases} \tag{1.7}$$

Let us consider a nucleus with odd number of nucleons (e.g. $A = 107$). In this case $\delta(N, Z)$ will be equal to zero and the equation (1.6) then gives quadratic relationship between the binding energy and the proton number. This can be seen in the figure 1.2a. Nucleus tends to undergo beta decay to reach the most stable isotope which is $Z = 47$ in this case. More interesting situation arises when considering nucleus with even number of nucleons (e.g. $A = 106$). In this case $\delta(N, Z)$ can either be $\frac{a_p}{\sqrt{A}}$ or $-\frac{a_p}{\sqrt{A}}$. Thanks to that we get two parabolas which can be seen in the figure 1.2b. The nucleus is decaying towards the most stable isotope. A spontaneous single beta decay transition to nucleus with $Z = 47$ is not possible because $Z = 47$ has a higher binding energy. The only way to reach more stable isotope is then directly to $Z = 47$ through double beta decay (red arrow in the figure 1.2b). Such isotopes where standard beta decay is forbidden are ideal to observe double beta decay since standard beta decay would otherwise produce very strong background.

1.2.2 Neutrinoless double beta decay ($0\nu\beta\beta$)

Neutrinoless double beta decay is a mode of double beta decay whithout the emission of neutrinos:

$$(A, Z) \rightarrow (A, Z + 2) + 2e^{-}. \tag{1.8}$$

It has been predicted by Wendell H. Furry in 1939 [9] but so far it has not been observed. Its existence would be possible if neutrino was a Majorana particle (its own

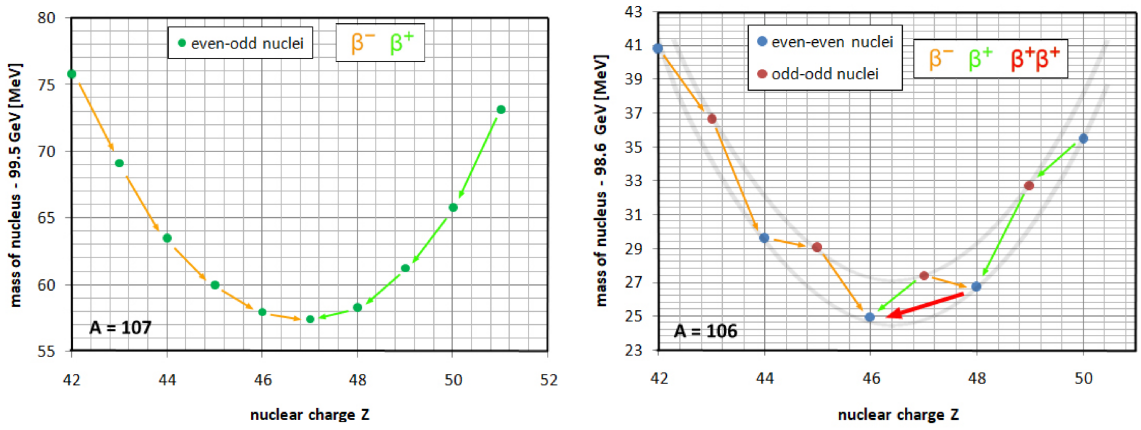

(a) (b)

Figure 1.2: a) Dependency of mass of nucleus with a mass number $A = 107$ on proton number Z. Green points represent individual isotopes, green and yellow arrows represent decays β^- and β^+. b) Same graph but for nucleus with $A = 106$. This time isotopes find themselves on two parabolas. Red arrow represents double beta decay. The figure was adapted from Volkmer [8].

antiparticle). This decay is not allowed by the SM since it violates lepton number conservation thus creating particles without equivalent amount of antiparticles. The existence of the $0\nu\beta\beta$-decay would mean a breakthrough in particle physics since it would imply Majorana nature of neutrinos. It could potentially lead us to physics beyond the SM and, finally, it would also help us to determine the mass of neutrino because its half-life is in direct relationship with neutrino mass:

$$\frac{1}{T^{0\nu}_{1/2}} = |m_{\beta\beta}|^2 \, G^{0\nu}(Q, Z) \left|M^{0\nu}\right|^2, \tag{1.9}$$

where $T^{0\nu}_{1/2}$ is half-life of $0\nu\beta\beta$-decay, $G^{0\nu}(Q, Z)$ is the phase-space factor, $|M^{0\nu}|$ is the matrix element of $0\nu\beta\beta$-decay and $m_{\beta\beta}$ is the effective neutrino mass defined as

$$m_{\beta\beta} = \sum_{i=1}^{3} U_{ei}^2 m_i, \tag{1.10}$$

where U_{ei} are elements of PMNS matrix (eq. 1.1) and m_i are mass eigenvalues. To determine the value of $m_{\beta\beta}$ we also need to know $G^{0\nu}(Q, Z)$ and $|M^{0\nu}|$ besides $0\nu\beta\beta$-decay half-life itself. While $G^{0\nu}(Q, Z)$ only depends on the Q-value and the proton number Z and can be calculated very precisely, $|M^{0\nu}|$ is a result of complicated nuclear models and brings more uncertainty into the equation. This, however, does not change the fact that $0\nu\beta\beta$-decay could potentially be used as a tool for neutrino mass estimation.

Principle of detection

The most significant background of $0\nu\beta\beta$-decay is the $2\nu\beta\beta$-decay. This is the main reason why we need to find a distinction between the two. In both cases we observe two electrons, the difference is, however, in their energy spectrum. In the case of $2\nu\beta\beta$-decay, the two neutrinos carry away fraction of the total released energy. The sum of

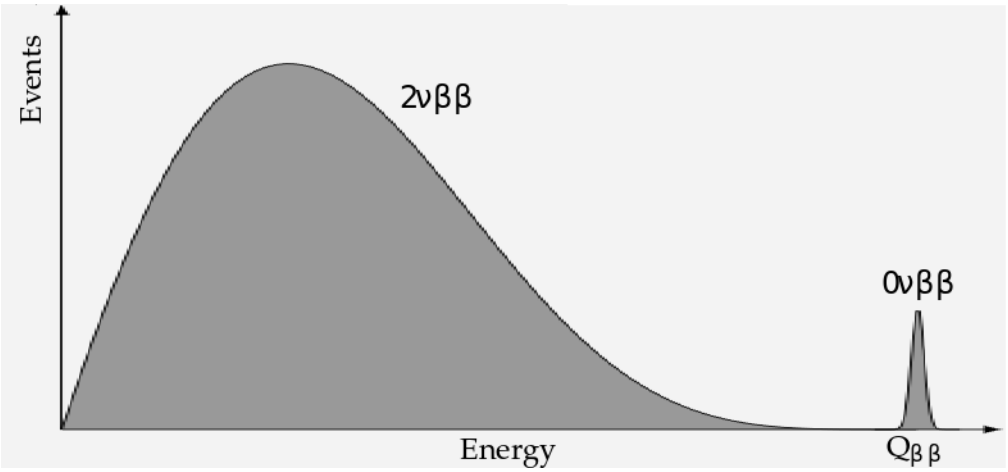

Figure 1.3: Comparison of $2\nu\beta\beta$-decay electron spectrum (left) and $0\nu\beta\beta$-decay electron spectrum (right). Observation of the sharp peak at the end of the spectrum would mean the existence of $0\nu\beta\beta$-decay. The figure was adapted from Macko [10].

the kinetic energies of electrons is equal to difference between Q-value of the decay and the kinetic energy carried by neutrinos. This results in a continuous spectrum (left spectrum in the figure 1.3). In comparison, during $0\nu\beta\beta$-decay there is no emission of neutrinos, so the energy of electrons is always equal to the Q-value. Which results in a sharp peak (right peak in the figure 1.3). Thanks to this, experiments search for the total energy deposited in the detector. If we would be able to recognize the peak at the end of the spectrum, we could confirm the existence of $0\nu\beta\beta$-decay.

1.3 Homogeneous detectors

Most $0\nu\beta\beta$ experiments use so-called homogeneous design where the part of the detector which provides energy measurement also contains an isotope which serves as the source of $0\nu\beta\beta$-decay. These experiments can be further divided based on the method of energy measurement.

First group of experiments uses semiconductor detectors. These typically use germanium diodes enriched of ^{76}Ge isotope which serves as the source of the decay. This approach is used by experiments GERDA [11] and MAJORANA [12].

Second group of experiments uses scintillation detectors. ^{136}Xe, which can be added to liquid or gas scintillators, is used as the source of the decay. In this group we have experiments KamLAND-Zen [13], EXO [14] or its successor nEXO [15].

Final group of experiments uses bolometers. These detectors contain a component which changes its resistance with small changes of temperature caused by energy deposition of $0\nu\beta\beta$ electrons. Based on these small changes the energy of the electrons can be measured. This approach is used by experiment CUORE [16].

1.4 SuperNEMO experiment

The SuperNEMO experiment is placed inside the LSM underground laboratory located in the middle of a traffic tunnel going through border between France and Italy (figure 1.4). Rock above the laboratory serves as a very effective shielding against cos-

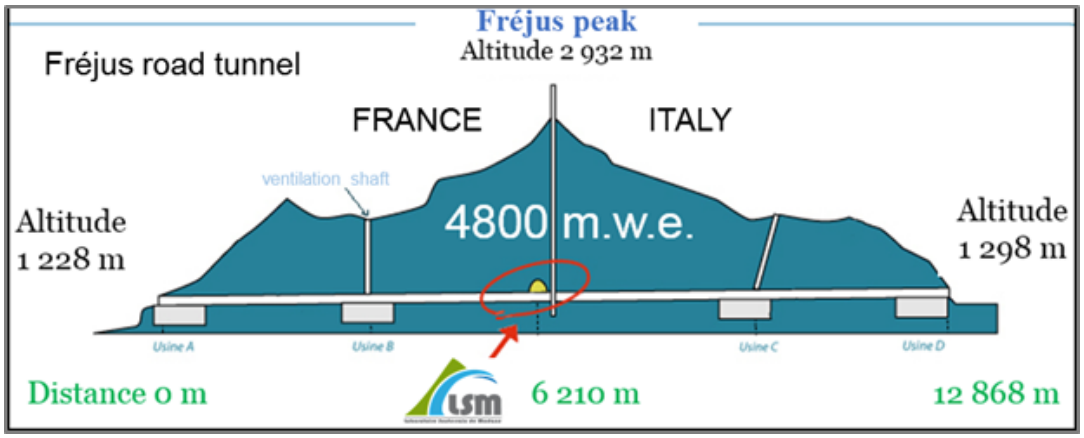

Figure 1.4: Scheme of the Fréjus traffic tunnel between France and Italy. LSM underground laboratory containing the SuperNEMO experiment lies approximately in the middle. The figure was adapted from Macko [10].

mic rays creating ideal environment for low background experiments. Currently, first SuperNEMO module called SuperNEMO demonstrator is in its commissioning phase.

SuperNEMO takes advantage of so-called tracko-calo design (figure 1.5a) which is unique in the field of double beta decay experiments as most detectors use homogeneous design. The design was validated by its successful predecessor NEMO-3 [17]. There are three main systems in the detector - source foil, tracker and calorimeter (figure 1.5b). Source foil serves as a source of $0\nu\beta\beta$-decay, tracker is used to measure trajectories of charged particles passing through the detector and calorimeter measures their energies. Whole detector is also surrounded by coil which can be used to create approximately homogeneous magnetic field inside the detector.

Both homogeneous and tracko-calo designs have their advantages. Homogeneous detectors are, in principle, simpler to design and they can use higher mass of the source isotope. These detectors, however, are not able to extract information about particle trajectories. Knowledge about trajectories allows us to perform full topological reconstruction of event and measure different properties of the decay such as angular distributions of electrons. It is also very useful for background event rejection because one can see whether the electron actually came from the source. In combination with the coil, we can also determine charge of particles based on curvature of their trajectory. At this point of commissioning, however, the coil is not switched on. The decision whether the magnetic field should be active during operation of the detector is still a point of discussion as the magnetic field could irreversibly influence parts of the detector through hysteresis.

1.4.1 Main detector systems

Source foil

The source foil contains 6.11 kg of ^{82}Se isotope serving as a source of $0\nu\beta\beta$-decay [19]. The thickness of the foil is only 0.3 mm. It is important to use a thin layer of the isotope to ensure that electrons will not lose too much energy in the source itself or even get absorbed. Several different isotopes have been considered to be used as a source from which ^{82}Se has been chosen since it meets multiple important criteria. First important thing is the Q-value of an isotope. Significant source of background is

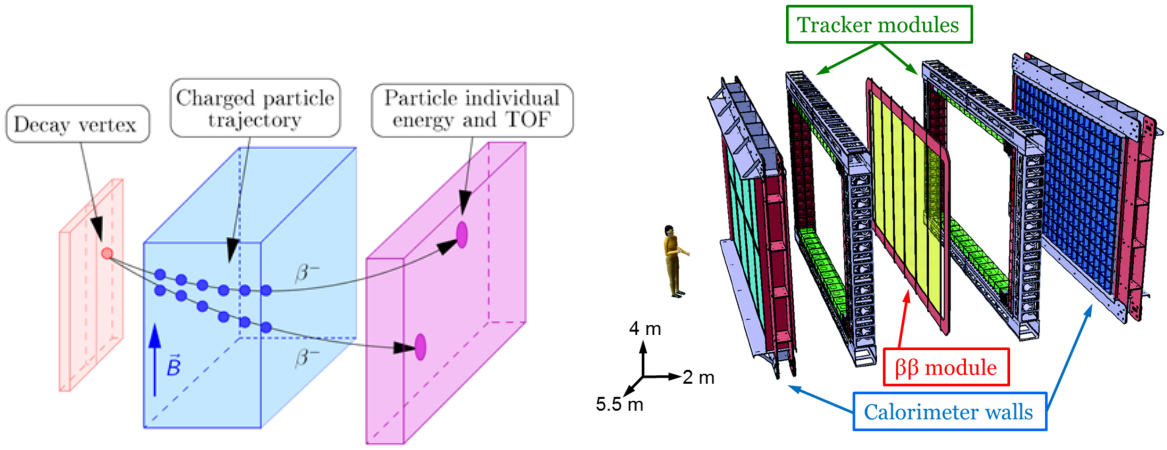

(a) (b)

Figure 1.5: a) Scheme of tracko-calo design. Rectangles represent $0\nu\beta\beta$-decay source (red), tracker (blue) and calorimeter (purple). b) Scheme of the SuperNEMO demonstrator. There is the source foil in the middle sandwiched by the tracker and the calorimeter. The figure was adapted from Barabash et al [18].

isotope ^{208}Tl. It decays through gamma decay emitting photons of energy 2.615 MeV. These photons can subsequently create electron-positron pairs which could mimic the signal of $0\nu\beta\beta$-decay. Q-value of ^{82}Se is 2.996 MeV which is high enough to recognize these electron-positron pairs from $0\nu\beta\beta$-decay electrons. Another source of background is the $2\nu\beta\beta$-decay (see the figure 1.3). It is, thus, important to choose an isotope with high $2\nu\beta\beta$-decay half-life. The value for ^{82}Se is $T_{1/2} = 0.87 \cdot 10^{20}$ years. Finally, we also need to choose an isotope which we are able to shape to the form of a thin foil.

Tracker

Tracker allows us to see trajectories of charged particles. It is a wire chamber with 113×9 drift cells on each side of the detector. Schematic view of a tracker cell can be seen in the figure 1.6b. Each cell consists of central high-voltage wire (anode) surrounded by 12 grounding wires. On each end of the anode there is a copper ring (cathode). The inside of the tracker is filled with gas (helium with 4 % of ethanol and 1 % of argon). Passing particles ionize the gas creating free electrons which can be attracted by electric field around anodes (figure 1.6a). While being pulled to an anode, electrons ionize another nuclei. This creates electron avalanches resulting in a measurable current signal. The time it takes for avalanche to reach the anode gives us an information about particle's distance from the anode. The signal then travels along the anode. Using difference of times when the signal hit the top and the bottom cathode we can calculate the height in which the particle passed.

Calorimeter

Calorimeter allows us to measure energies of electrons coming from the $0\nu\beta\beta$-decay - the main quantity of interest. The whole calorimeter is segmented and consists of 712 so-called optical modules (OMs; figure 1.7b). These modules are placed in two main walls parallel to the source foil ("mwall") as well as above and bellow ("gveto") and on the sides of the source foil ("xcalo"). Each optical module is a scintillation

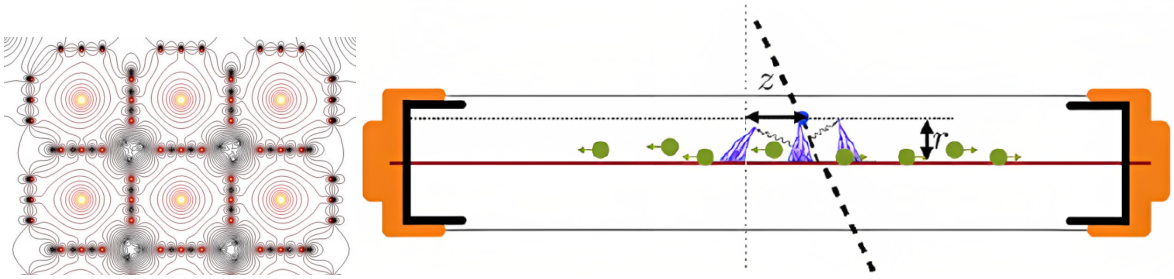

(a) (b)

Figure 1.6: a) Electric field in tracker cells. (top view) b) Side view of a tracker cell. There is a high-voltage wire (anode) in the middle and copper rings (cathodes) on its and. The dashed line represents passing particle which caused an avalanche of electrons and consequential propagation of plasma along the anode. Height z and distance from wire r can be calculated from measured signal. Courtesy of Cheryl Patrick (SuperNEMO collaboration).

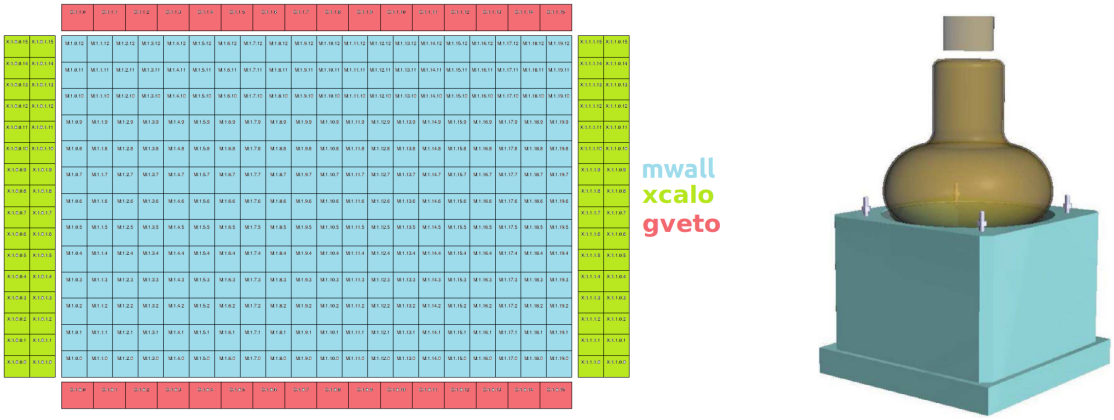

(a) (b)

Figure 1.7: a) Scheme of one half of the calorimeter unwrapped into a plane. It consists of individual optical modules which we devide into three groups - "mwall", "xcalo" and "gveto". b) Optical module consisting of a photomultiplier tube and a block of scintilator.

detector consisting of a photomultiplier tube (PMT) and a block of plastic scintillator (polystyrene; figure 1.7a). The "xcalo" and "gveto" OMs are reused from the previous experiment NEMO-3. They use 5" PMTs and their resolution is 12 % at 1 MeV for "xcalo" and 15 % at 1 MeV for "gveto". OMs used in the main walls use 8" PMTs and their scintillator blocks contain two additional substances improving light collection efficiency of PMT: 0.6 % of para-terphenyl (pTP) and 0.05 % of 1,4-bis(5-phenyloxazol-2-yl) benzene (POPOP). Several concentrations of these additives have been tested to find the optimal one [20]. Thanks to that the main wall modules reach resolution of about 8 % at 1 MeV.

1.4.2 Calorimeter calibration

Before we can start to measure energies of electrons and to look for the peak at the end of double beta decay spectrum (figure 1.3) we need to calibrate the calorimeter.

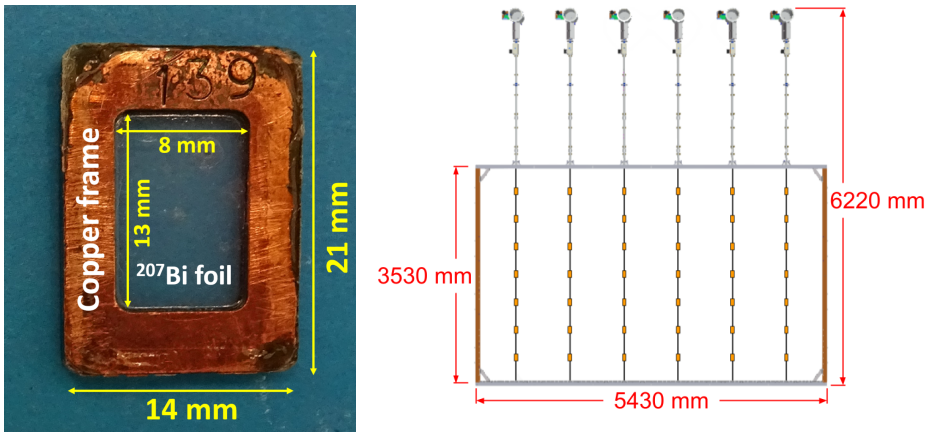

(a) (b)

Figure 1.8: a) A ^{207}Bi calibration source consisting of a mylar foil, a copper frame and a small droplet of ^{207}Bi in the middle (not visible). b) Automatic deployment system used to position the calibration sources in the middle of the detector. The figure was adapted from Arnold et al [19].

Since a sufficient energy resolution is a key element of the experiment, high precision of the calibration will also be crucial. It is important to realize that properties of individual OMs will slightly differ as well as they will slowly change with time. Therefore, it is necessary to calibrate each OM individually and to perform the calibration measurements periodically in sufficient time intervals.

Calibration system

The calibration measurement will be performed using a system of 42 calibration sources. Each source contains small droplet of ^{207}Bi sandwiched between two transparent mylar foils. The foils are stretched into a copper frame so that the ^{207}Bi droplet is in the middle (figure 1.8a). The positions of the ^{207}Bi droplets have been measured to ensure that they did not leak under the frame [19]. Before the calibration measurement we need to place the calibration sources on chosen positions inside the detector. These positions should be the same for each calibration measurement. During this process the detector also must stay sealed so that there are no leaks of the tracking gas. To place the sources in the middle of the detector an automatic deployment system has been built (figure 1.8b). This system consists of 6 rods connected to stepper motors using which we can place the calibration sources on precise positions along the source foil.

Principle of the calibration

^{207}Bi atom can undergo so-called internal conversion (IC) - a process during which an excited nucleus transfers its energy to one of the orbital electrons. This results in emission of the electron and an X-ray. The electron can come from any of three electron shells commonly referred to as K, L and M-shells, where K is closest to the nucleus having the highest probability of IC and M is the most distant one with the lowest probability of IC. Since the excitation energies of the nucleus are discrete as well as ionisation energies of electrons from different shells, the spectrum of IC electrons is

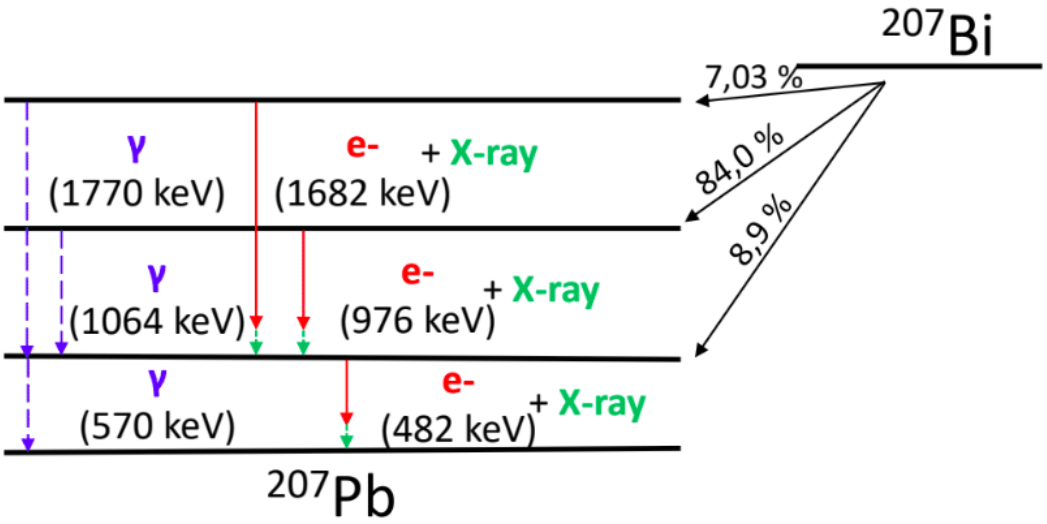

Figure 1.9: A simplified decay scheme of ^{207}Bi containing the most frequent transitions. ^{207}Bi can emit gamma rays through gamma decay or electrons and X-rays through internal conversion.

also discrete. In the figure 1.9 we can see a simplified decay scheme of ^{207}Bi containing IC electrons from the K-shell. This is very useful for the calibration because we can detect these electrons using optical modules and find a relationship between known energies of IC electrons and a charge collected in the optical module.

Chapter 2

Calibration data analysis

2.1 Simulated data

In order to perform simulations SuperNEMO collaboration uses its own simulation system called Falaise [21]. The system is based on Geant4 package developed in CERN [22]. Falaise contains information about geometry of the detector, properties of its parts, different types of decays, etc. It also offers a simple user interface which contains a range of options from which a user can choose to set up a simulation. Thanks to this, the setup of a simulation is very quick and convenient.

For standard use, Falaise offers 3 programs - flsimulate, flreconstruct and flvisualize. Flsimulate simulates passage of particles through the detector. It produces information about particle interactions in materials and about energy deposited in different points of particle's trajectory. Flsimulate gives us the absolutely precise information about particles which we do not have in case of real measurement. An output of Falaise simulation comes in a form of so-called "brio" file. Inside this file, data are divided into data banks. Data produced by flsimulate are saved in SD bank (Simulated Data). It contains information about particle types, energies, trajectories and individual interactions.

Data produced by flsimulate can be further processed by flreconstruct. A run of flreconstruct consists of pipeline modules. These modules can perform different tasks from printing the data to complex analysis. A user can use predefined modules as well as define new ones to customize data processing. The main purpose of flreconstruct is to provide response of the detector based on data produced by flsimulate. The output of flreconstruct is another "brio" file. This file contains the SD bank previously produced by flsimulate as well as 4 other banks. First of them is CD bank (Calibrated Data). This bank contains quantities detected by different parts of the detector including their uncertainties. Then there are TCD (Tracker Clustering Data) and TTD (Tracker Trajectory Data) banks. TCD contains informations about clusters of tracker hits. These clusters should correspond to tracks of individual particles. From these clusters trajectories of individual particles are extracted using so-called CAT algorithm (Cellular Automaton Tracker). These trajectories are saved into TTD bank. Finally there is PTD bank (Particle Track Data) which contains information reconstructed from its trajectory. These are charge of the particle and vertices at the start and at the end of the trajectory.

The third Falaise program called flvisualize is used to visualize data produced by flsimulate and flreconstruct. An example of such visualization can be seen in the figure

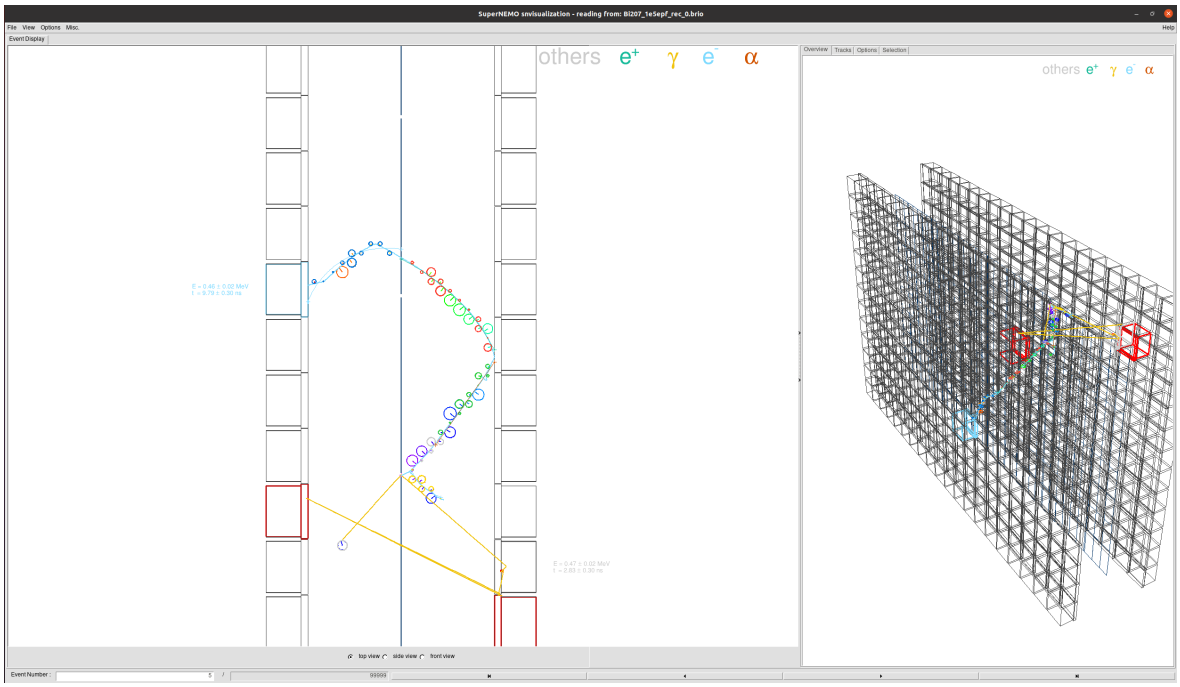

Figure 2.1: Flvisualize visualization of a single event. We can see the source foil in the middle of the detector, tracker hits represented by colored circles and OMs represented by black rectangles.

2.1. The main benefit of flvisualize is that it allows us to gain an intuition about data and to check whether the simulation behaves as we expect.

2.2 Real data

During the real measurement, SuperNEMO uses complex system of electronics to extract signals from the tracker and the calorimeter. Since saving continuous signal from the whole detector would be very inefficient, SuperNEMO uses trigger system to decide when to keep the data. Trigger looks for time and space coincidence between signal from the tracker and the calorimeter. Once the trigger condition is met, signal from whole detector (measured during a small time window around the trigger time) is saved. A unique trigger ID is assigned to these data. Signals from both the tracker and the calorimeter have characteristic waveforms which are used to extract information about particle's trajectory and energy.

2.2.1 Tracker signal

A tracker cell consists of three parts - anode, top cathode and bottom cathode (see the figure 1.6b). Each of these parts provides its own voltage signal. Since voltage waveforms have variable amplitudes we cannot define a single voltage threshold. Because of that it is more convenient to work with derivatives of these waveforms. An example of the differentiated cathodic signal can be seen in the figure 2.2. In the figure we can see two timestamps t_5 and t_6. t_5 always corresponds to bottom cathode and t_6 to top cathode regardless of which waveform comes first. Using these two timestamps and the speed of plasma propagation along the wire we can calculate height in which the

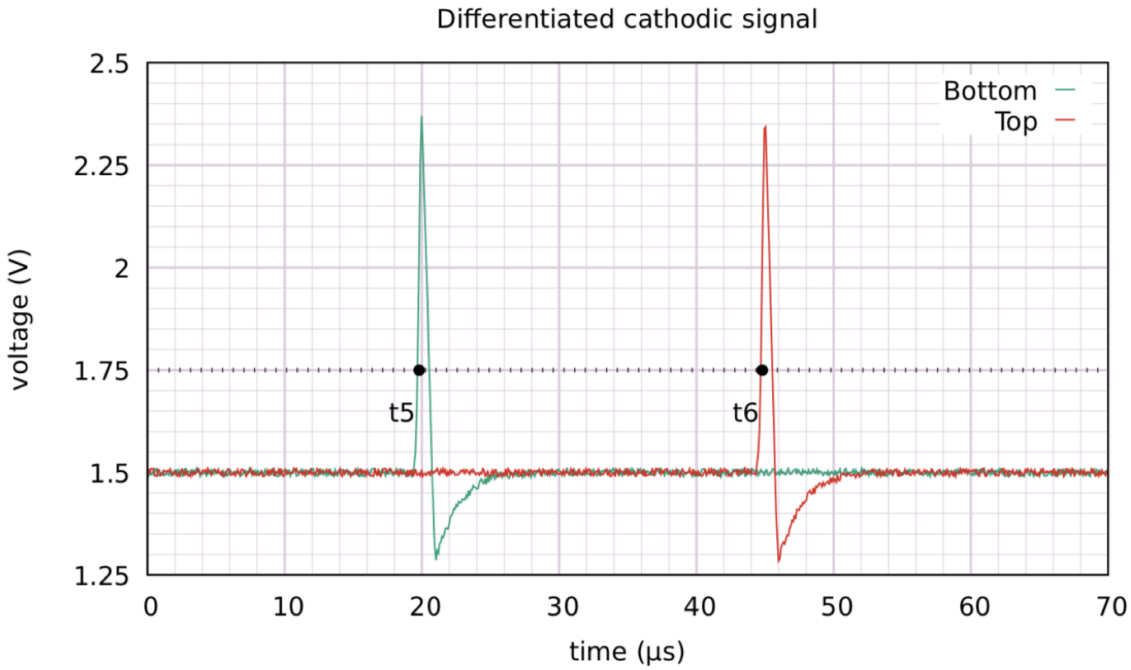

Figure 2.2: Differentiated cathodic signal. We can see two timestamps t_5 and t_6 corresponding to times when plasma reaches the bottom and top cathode. Courtesy of SuperNEMO collaboration.

particle passed the tracker cell. Besides that we also get the signal from the anode. Differentiated anodic signal can be seen in the figure 2.3. Here we have 5 different timestamps t_0 to t_4. These are always sorted chronologically. Timestamps t_1 and t_3 correspond to the earlier cathodic timestamp (either t_5 or t_6) and timestamps t_2 and t_4 correspond to the later one. We can see that t_1 to t_4 represent the same information which we extract from the catodic signal. The only difference is that purely from anodic signal we are not able to distinguish which pulse corresponds to the bottom of the anode and which corresponds to the top. Thanks to this redundancy we are able to calculate the height of the particle even if we only have signal from anode and one cathode. The most important information is provided by t_0. This is the drift time of electrons coming form the point of ionization to the anode. We can extract the distance in which the particle passed the anode from value of t_0 using so-called drift model. Drift model is based on the shape of electric field around the anode and describes the relationship between t_0 and the distance from the wire. Developing a reliable drift model is not a trivial task and it is still studied by members of SuperNEMO. Two drift models have already been developed and are used in data processing.

2.2.2 Calorimeter signal

A typical waveform recorded by an OM when hit by a particle can be seen in the figure 2.4. Integral of the waveform is proportional to the total charge collected in the OM during interaction with the particle. This charge is in relationship with the energy deposited in the OM. Finding this relationship is the goal of the calibration.

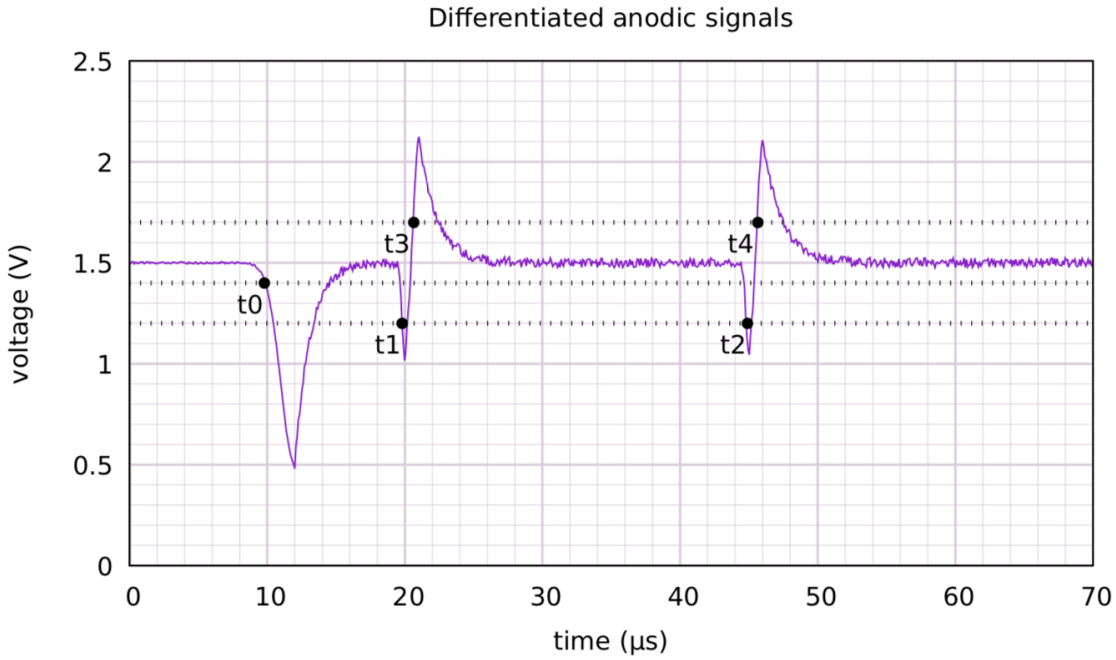

Figure 2.3: Differentiated anodic signal. t_0 represents the drift time and t_1 to t_4 represent times when plasma reaches the bottom and top cathode. Courtesy of SuperNEMO collaboration.

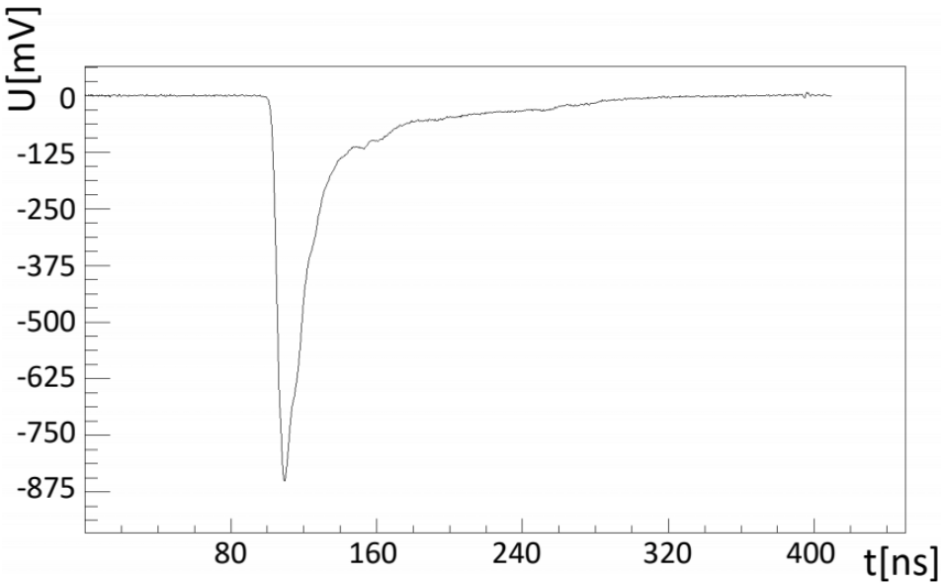

Figure 2.4: An example of waveform captured by an OM. Integral of the waveform corresponds to the energy of the particle.

2.2.3 SuperNEMO data formats

SuperNEMO uses a number of data formats to save and process data. These range from unstructured and simple ones used during the data acquisition (DAQ) to more structured ones which should provide a clear representation of the data suitable for data analysis.

Commissioning binary data (CBD)

Raw signals from the SuperNEMO detector are processed by so-called SNCrateSW DAQ software which produces data files in what we call Commissioning Binary Data format. Data from the detector come in 6 data streams resulting in 6 CBD files. Each file comes from one DAQ crate (3 from tracker, 3 from calorimeter). Signals in this format are not ordered by time nor their trigger ID. CBD are, however, very compact, optimized for the DAQ and serve as a basis for more structured formats.

Raw hit data (RHD) and Raw trigger data (RTD)

6 CBD files obtained during measurement run are later converted into 6 Raw Hit Data files. Each of these files contains signals from one part of the detector sorted by their trigger IDs. These 6 files are then converted into one Raw Trigger Data file. This file contains signals from the whole detector sorted by their trigger ID. This format represents signals as they are registered by readout electronics after a trigger. RTD format can already be used for data analysis, but it still contains some low-level information. It is more suitable for diagnostic of DAQ rather than for complex analysis tasks.

Raw event data (RED)

Finally, RTD file is converted into Raw Event Data using algorithm which looks for triggers in a small time window and merges data with different trigger IDs into events based on their time coincidence. The idea is that these events provide similar data structure as events produced by simulation software Falaise. This makes working with RED files very natural for people previously working with simulations. Currently, RED is the data format used for most of the data analysis.

Future formats

Even though the RED format provides very similar data structure to files produced by Falaise simulations, the way of handling simulated and real data is still different. In the future a new pCD (pre-Calibrated Data) format should be developed. It will have the same structure as "brio" file with CD bank but contain measured data. Using calibration parameters of the detector pCD will be transformed into CD bank containing same quantities which we get from simulations. Future versions of Falaise should also include running conditions of the detector (eg. damaged tracker cells) as well as an option to simulate analog signal produced by the detector which would be comparable with the real data. On the other hand, DAQ will include calibration parameters giving us the relationship between charge measured by the calorimeter and energy of the particle.

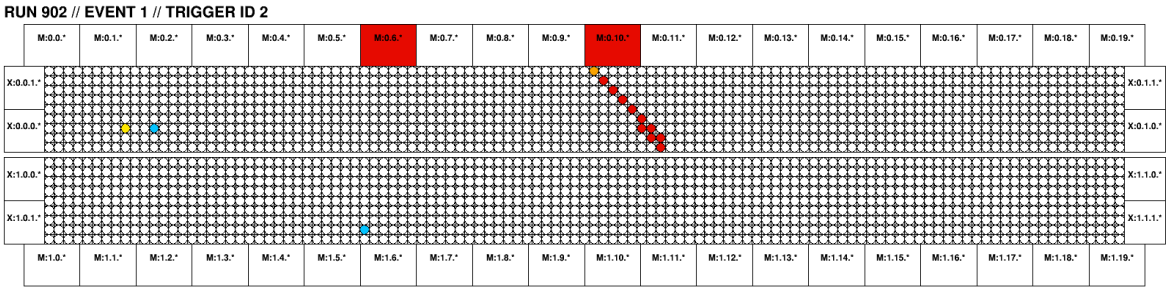

Figure 2.5: An example of ^{207}Bi calibration event. Colored circles represent tracker hits. Red rectangles represent triggered OMs.

2.3 Calibration data and event selection

2.3.1 Event

Data files in the RED format (described in the previous section) were used for analysis throughout the whole work. We can see an example of a typical event in the figure (2.5). Each event contains tracker hits and OM hits. A tracker hit gives us an information about signal captured by a single tracker cell. It consists of tracker cell ID and timestamps extracted from anodic and cathodic signal (figures 2.2 and 2.3).

OM hit contains OM ID, time when the OM was triggered and information about measured waveform. The integral of the waveform is calculated to extract total collected charge which gives us an information about particle's energy. The time from the OM is also useful since we can compare it with timestamps from tracker hits and calculate the distances in which the particle passed different tracker cells.

2.3.2 Event selection

Even though, the SuperNEMO detector was carefully constructed with emphasis on the background reduction, there are obviously still sources of radiation other than ^{207}Bi. Because of that we need an algorithm able to select the events containing an electron from calibration source hitting an OM and to filter out background events. In the following section three different selection algorithms will be described chronologically as they were developed.

Naive event selection

Our goal is to find events with track coming from a calibration source to a triggered OM. The easiest way to do this, is to simply check all tracker cells near calibration sources and tracker cells in front of all triggered OMs. We, thus, proceed in two steps:

1. Check one row of tracker cells on each side of the calibration sources. If there is at least one hit, we continue to the next step.

2. Check tracker cells which are directly in front of each triggered OM (6 or 7 cells based on the position of the OM). If there is at least one hit, save charge measured by given OM.

In the figure 2.6 we can see an example of event which would be accepted.

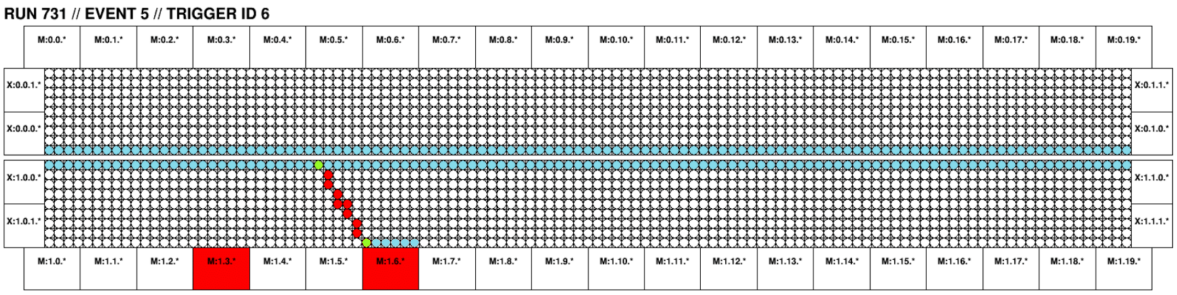

Figure 2.6: An example of event accepted by naive event selection algorithm. Blue cells are the ones which were checked for hits. Since there were tracker hits in checked regions (green cells), the event is accepted.

2D tracking

The naive event selection algorithm can easily misclassify events mainly because it does not look for tracker hit clusters making up tracks but it only checks areas of the tracker for single hits. This way we cannot really recognize if there was an electron traveling from a calibration source to an OM or if there were only few random tracker hits which made the event pass.

A better way to look for calibration electron is to first find a track corresponding to measured tracker hits. In other words, we fit a straight line through cluster of tracker hits which represents the most probable track of the particle which triggered these tracker cells. The task of finding the most probable track based on tracker hits is very complex and efficient algorithms able to solve it are still in development. In this work, we will use an algorithm based on Legendre transform which is currently being developed by Tomáš Křižák (member of SuperNEMO collaboration) [23] [24]. The first version of the tracking algorithm was restricted to search for a track in horizontal plane without considering the vertical coordinate. This can cause ambiguity in deciding which of the OMs in the same column intersects with the track, however it still provides a much better way of recognizing calibration electrons than the previous algorithm. Using tracking we can update our selection algorithm:

1. Extract parameters a and b (slope and intercept in horizontal plane) of the track line.

2. Calculate initial vertex of the track as an intersection between the track line and the plane where the calibration sources are positioned.

3. Calculate final vertex of the track as an intersection between the track line and the calorimeter.

4. Check whether the distance between the initial vertex and the closest calibration source is lower than d_1.

5. Check whether the distance between the final vertex and the front face center of the closest triggered OM is lower than d_2.

6. If conditions 4 and 5 are met, save charge measured by OM closest to the final vertex.

	D1 Acceptance[%]	D2 Acceptance[%]
Naive Selection	72.51	45.34
2D Tracking	48.68	13.66
3D Tracking	51.15	4.00

Table 2.1: Acceptance rates of three different event selection algorithms applied on datasets D1 and D2.

Distances are calculated only in horizontal plane because we do not know the vertical coordinate of the track. Values d_1 and d_2 influence the efficiency of the selection. For demonstration purposes they were chosen as $d_1 = 10$ cm and $d_2 = 15$ cm. In the final calibration software the parameters of the selection algorithm will be optimized.

3D tracking

Even though the 2D tracking algorithm is an improvement compared to the naive event selection, it is incomplete if we do not take vertical coordinate into account. A new version of the tracking solves this problem. Using 3D tracking we can apply the same algorithm as the previous one, but we calculate the distances in 3D. This way we can also differentiate between individual OMs in one column.

Algorithm comparison

Real data analysis presented in this work takes advantage of two datasets. Both datasets contain 12 hours of measurement. In the first dataset (D1) calibration sources were deployed inside the detector. In the second dataset (D2) calibration sources were removed and only background was measured. D1 is from detector runs 763 to 770 and D2 is from runs 777 to 779. D2 is useful to determine how many background events are accepted by different selection algorithms and also to subtract the background from the results obtained from D1. In both datasets only the middle part of the tracker was active so we only get signal from the middle part of the detector.

Each of the three selection algorithms have been applied on datasets D1 and D2. We can see acceptance rates of all selection algorithms in Table 2.1. Naive selection accepts more than 45% of background events and 72.5% of events from D1 being very bad in recognizing signal from background. 2D tracking offers an improvement but its acceptance rate for D2 is still high. 3D tracking accepts only 4% of background events while accepting slightly more events from D1 than 2D tracking so it is much better at background discrimination. In the figure 2.7 we can see comparison of spectra from two different OMs obtained using different selection algorithms. We can see that in case of naive selection, the first peak is deformed by high number of accepted background events while in case of 2D tracking the first peak is clearer but the second peak is suppressed. 3D tracking results in relatively clear first peak while preserving the second peak.

2.3.3 Comparison of simulation with real data

In previous work [6](in Czech), a study of calibration measurement properties was performed using Falaise simulations. The main point of this study was the calibration spectrum measured by individual OMs - mainly its shape and electron rates in OMs.

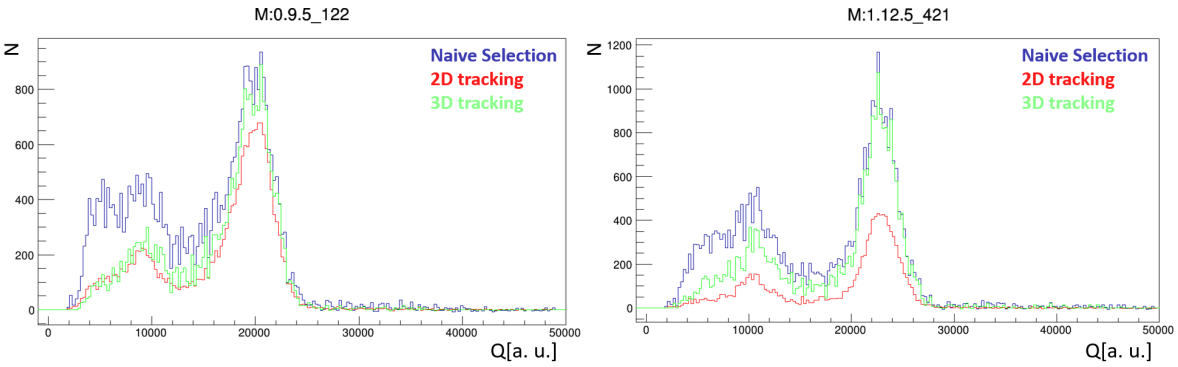

Figure 2.7: Comparison of spectra measured by two OMs obtained using three different selection algorithms. 3D tracking performs the best filtering out most of the background events while not suppressing signal too much.

Using newly obtained real data, we can verify the predictions made by the simulation. Only results obtained using the 3D tracking will be shown in the following comparisons as it has the best performance.

Optical module exposure

Knowledge of electron rates impacting individual OMs is a valuable information. It helps us to estimate calibration measurement duration necessary to reach desired statistics for calibration. A preliminary estimate of OM exposures has been made in the past based on simulated data. Real exposures were calculated using 3D tracking for datasets D1 and D2. Then exposures from D2 were subtracted from the ones from D1 to remove contribution of the background. In the figure 2.8 we can see ratio between real exposure and simulated one for each OM. We can see that most ratios are lower than one. This tells us that we generally got higher exposures from the simulation. Lower values obtained from real data are probably caused by the fact that different tracking algorithm was used for simulation.

Calibration spectrum

Understanding of the shape of the calibration spectrum measured by OMs and effects which influence it is crucial to achieve precise calibration and to ensure high sensitivity of the detector. In the figure 2.9, we can see comparison between calibration spectrum from simulation and from real data (background obtained from D2 was again subtracted). They correspond to different lengths of measurement which is why absolute amplitudes of the peaks differ. We are, however, interested in shape of the peaks, so absolute amplitudes are not relevant at the moment. As we can see, the x-axis of simulated spectrum is in keV while x-axis of real spectrum is in units of charge. Finding the relationship between measured charge and energy of a particle is the goal of the calibration. We could already extract calibration parameters by assigning energy of 482 keV to the first peak in the charge spectrum and energy of 976 keV to the second one. Such calibration would however be very imprecise without understanding effects which influence position and shape of the peaks. It would not give us any useful information at this point, so we leave the real spectrum in units of charge.

There are two main differences between the simulated spectrum and the real one. The first difference is in shape of the first peak. In the simulated spectrum the slope

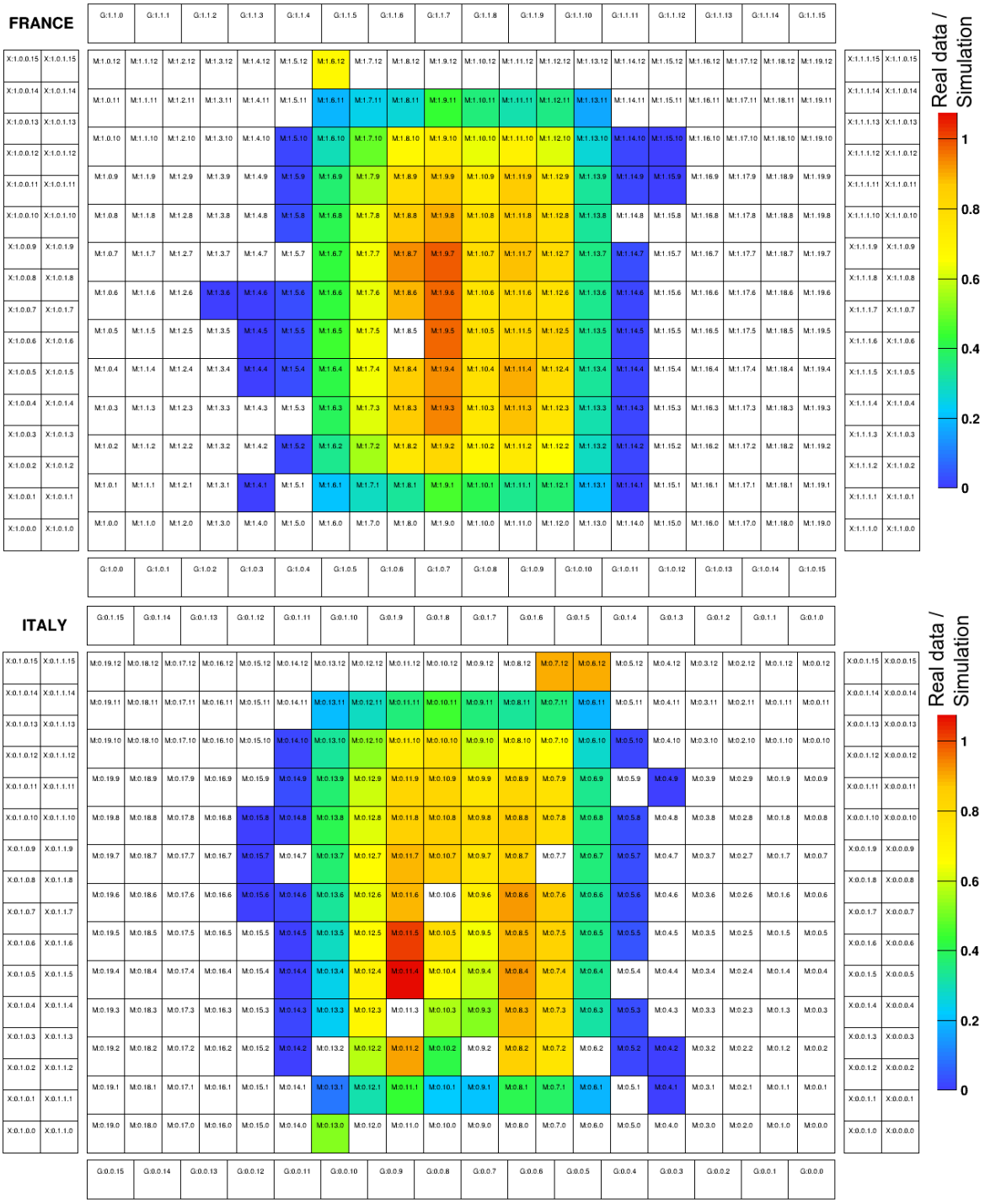

Figure 2.8: Comparison of OM exposures obtained from the simulation of from the real data. Color represents ratio ratio between simulated and real exposure for each OM.

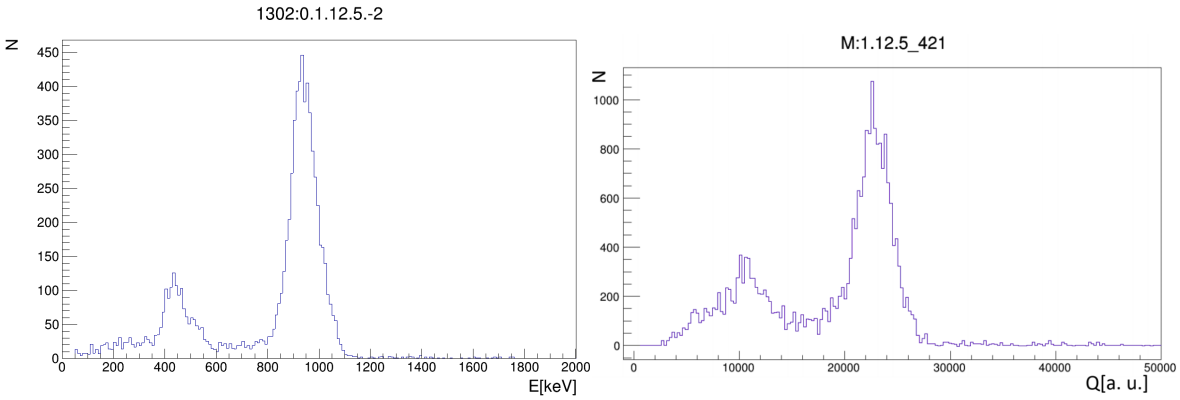

(a) (b)

Figure 2.9: Comparison between calibration spectrum of single OM obtained from simulation(a) and from real data(b).

on the left side of the peak is significantly higher than in the real spectrum. This is probably caused by current configuration of the detector. The second difference is in ratio between amplitudes of the peaks. In simulated spectrum second peak is 4 times higher than the first one. In the real spectrum it is only about 3 times higher.

2.3.4 Calibration spectrum corrections

Shape of the calibration spectrum is influenced by different effects. Some of them can be described and compensated. Currently, two models with goal to describe these effects are in development. These are optical correction and energy loss correction.

Optical correction

As described in the chapter 1 OMs consist of a scintilator block and a PMT which collects light emitted by the scintilator when hit by a particle. It turns out that the signal produced by PMT is dependent on the point where the particle deposits its energy because the light collection is dependent on where it was emitted. So-called geometrical correction has been developed by group from University of Bordeaux (SuperNEMO collaboration) to describe this geometrical dependence of PMT signal [25] [26]. Values of geometrical correction factor for different points on OM front face can be seen in the figure 2.10. Furthermore, fast particle moving through the scintilator emits Cherenkov radiation. Because of that, the number of photons emitted in the scintilator does not increase linearly with the energy of the particle. This effect also needs to be taken into account. Finally, Birks' law describing light yield as a function of the energy loss per path length also has to be considered. It has a form [27]

$$\frac{dS}{dr} = \frac{A\frac{dE}{dr}}{1 + k_B\frac{dE}{dr}}, \tag{2.1}$$

where $\frac{dS}{dr}$ is light yield per path length, $\frac{dE}{dr}$ is energy loss per path length and A and k_B are constants specific for material of the scintillator. As we can see for low values of $\frac{dE}{dr}$ $\frac{dS}{dr}$ is simply a linear function of $\frac{dE}{dr}$ (see the figure 2.11). However, for high $\frac{dE}{dr}$ $\frac{dS}{dr}$ saturates.

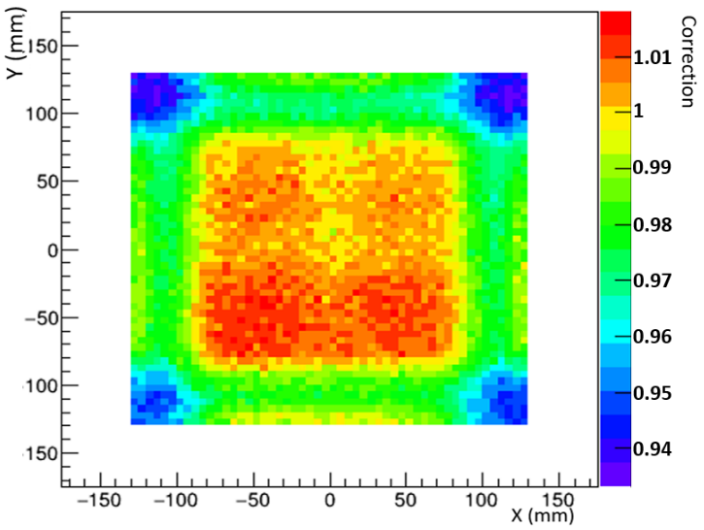

Figure 2.10: Map of geometrical correction factor for front face of an OM. We can see that the correction is most significant on the edges of the OM. The figure was adapted from Pin [26]

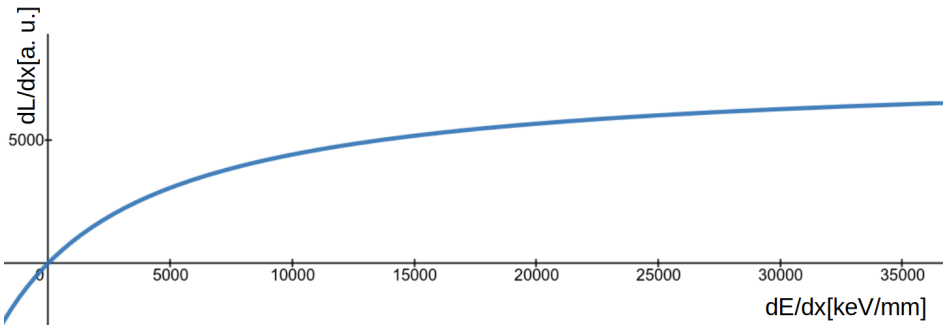

Figure 2.11: Relationship between energy lost per path length and light yield per path length in a scintilator according to the Birks' law. It saturates for high $\frac{dE}{dx}$.

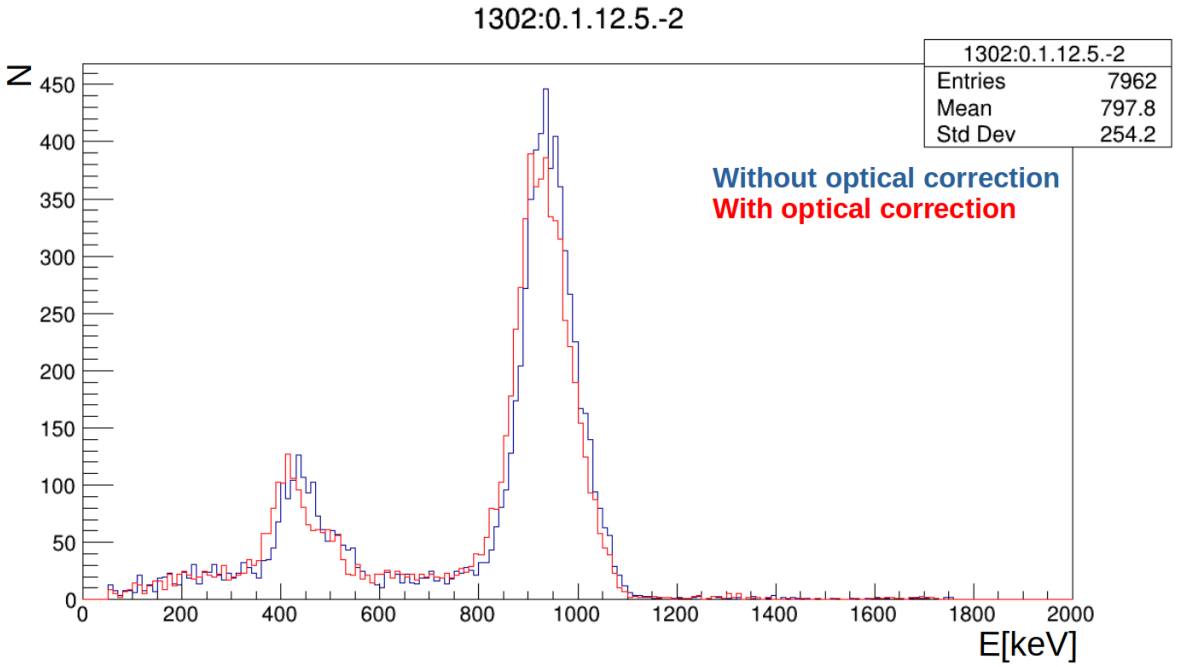

Figure 2.12: Comparison of simulated spectra with and without the effect of optical correction. We can see the ratio of amplitudes of the second and first peak slightly decreased getting closer to the ratio from the real data.

Corrections for the three mentioned effects (geometrical non-uniformity, Cherenkov radiation and Birks' law) are combined into one model referred to as optical correction. Optical correction has already been implemented in simulation software Falaise so we can generate simulated data with its effects applied on energies measured by OMs. In the future, it will also take part in the fitting algorithm which will be used in the calibration software.

Using newer version of Falaise (4.1.0 alpha), in which the optical correction has been implemented, we have recreated simulation of the calibration measurement. In the figure 2.12 we can see comparison between energy spectrum from figure 2.9 and the spectrum we got after application of the optical correction. After application of the correction, the peaks are slightly wider and the amplitude of the second peak slightly decreased. The ratio between amplitudes of the peaks is now closer to the real data, however, it is still higher. It is probably due to the fact that the resolution of real OMs is worse than in the simulation. Worse resolution results in wider peaks and lower ratio between the amplitudes.

Energy loss correction

While the optical correction describes effects which emerge during the interaction between an electron and the OM, there is another factor to take into account even before the electron reaches the OM. The electrons lose part of their energy in the tracking gas before they reach the calorimeter. If we were to calibrate expecting peaks in the charge spectrum to correspond to 482 and 976 keV we would get very imprecise results because electrons actually have lower energies when they hit the calorimeter. Moreover, this effect of energy losses also makes peaks in the spectrum wider which results in lower precision of the calibration (we cannot locate them as precisely). To account for these

p_1	$(0,166 \pm 0,008)$ keV $\cdot$ mm^{-1}
p_2	(-42 ± 5) keV
p_3	$(3,40 \pm 0,04) \cdot 10^{-3}$ keV^{-1}
p_4	$(6,82 \pm 0,06) \cdot 10^{-2}$ keV $\cdot$ mm^{-1}
p_5	$(-5,2 \pm 0,4)$ keV

Table 2.2: Parameters of energy loss correction (2.2).

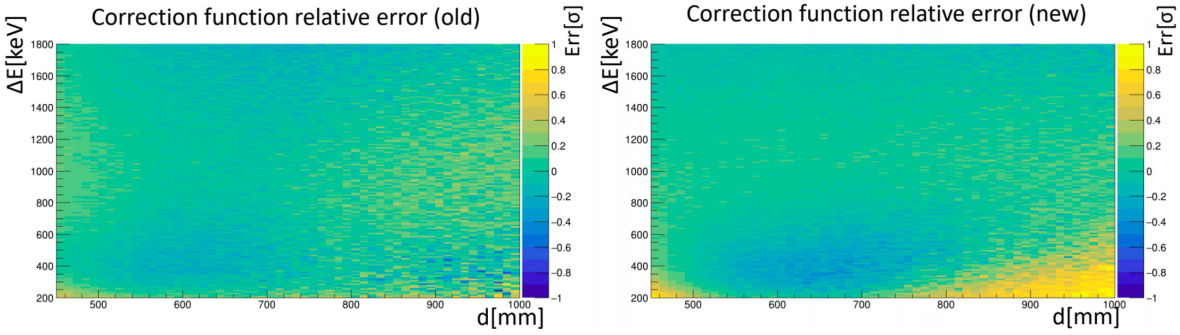

Figure 2.13: Comparison of fitting error obtained by fitting formula (2.2) to two different datasets. New dataset differs from the old one in absence of magnetic field inside the detector and by using different tracking algorithm.

losses an energy loss correction has been developed in previous work[6](in Czech).

The correction function has form

$$\Delta E(E_f, d) = (p_1 d + p_2) e^{p_3 E_f} + p_4 d + p_5, \tag{2.2}$$

where ΔE is energy lost by an electron while traveling through the tracking gas, E_f is energy of an electron when it hits an OM, d is distance between initial and final vertex of electron trajectory and values of parameters p_1 to p_5 are in Table 2.2. The correction was developed using Falaise simulation of electrons of different energies generated from calibration sources. Formula (2.2) is purely empirical and was proposed simply to fit the simulated data. This approach, however, has several problems. First of all, using 5 parameters may be unnecessary and the number could probably be reduced using more sophisticated model. Also, current parameters do not have any physical interpretation. It would be better to have model with parameters directly related to properties of the detector. Finally, energy loss analysis leading to formula (2.2) was performed using older tracking algorithm and simulation where magnetic field inside the detector was active. This is in contradiction with the real data since detector operates without magnetic field and different tracking algorithm is used. We repeated the simulation without magnetic field and with newer tracking algorithm. Fitting this new simulated data with function (2.2) resulted in higher error than in case of older data. We can see comparison of fitting errors in the figure 2.13. Especially for lower energies (200 - 800 keV) there is higher systematic error when fitting the new simulated data.

Flaws of formula (2.2) lead us to conclusion that new theory-based correction should be developed. As electrons travel through the tracker they ionize atoms of the tracking gas. This process is the main source of energy losses. Ionization losses of charged particles are described by Bethe-Bloch formula[28]

$$-\left\langle \frac{dE}{dx} \right\rangle = \frac{4\pi}{m_e c^2} \cdot \frac{nz^2}{\beta^2} \cdot \left(\frac{e^2}{4\pi\varepsilon_0} \right)^2 \cdot \left[\ln\left(\frac{2m_e c^2 \beta^2}{I \cdot (1-\beta^2)} \right) - \beta^2 \right], \tag{2.3}$$

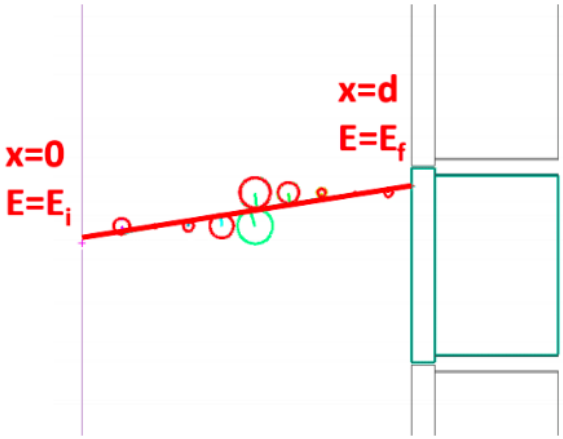

Figure 2.14: A scheme of electron traveling through the tracker. It has energy E_i at initial point $x = 0$, then it passes distance d along which it losses energy through ionization. At the end of the trajectory it has energy E_f.

where $\left\langle \frac{dE}{dx} \right\rangle$ is mean lost energy per distance traveled, m_e is electron rest mass, c is the speed of light, β is the relativistic factor($\beta = \frac{v}{c}$), e is elementary charge, z is charge of the particle (in multiples of e), ε_0 is vacuum permittivity, I is mean excitation energy of the tracking gas and n is electron density of the tracking gas which can be calculated as

$$n = \frac{N_A \rho < Z/A >}{M_u}, \tag{2.4}$$

where N_A is the Avogadro constant, M_u is molar mass of the tracking gas and $< Z/A >$ is average ratio between atomic number and relative atomic mass. A scheme of our energy loss problem is in the figure 2.14. We can see an electron which passes distance d. At the start of its trajectory it has energy E_i and at the end its energy is E_f. We are trying to predict $\Delta E = E_i - E_f$. Both E_f and d can be measured. E_i is, thus, the unknown. Energy losses of electron between $x = 0$ and $x = d$ are described by (2.3). This leads us to a problem of solving differential equation with boundary conditions $E\,(0) = E_i$ and $E\,(d) = E_f$. We can simply integrate the equation (2.3) to get

$$\int_{E_f}^{E_i} \frac{dE}{f\,(E)} = d, \tag{2.5}$$

where $f\,(E)$ is the right side of the equation (2.3). From this equation we would like to express E_i. Unfortunately, finding analytical solution for the integral on the left side does not seem to be possible. The equation needs to be solved either numerically or using approximations. Finding the solution is, however, out of scope of this work.

Another possible approach is to describe energy losses using Landau distribution. It describes the probability distribution of lost energy of particles with fixed initial energy passing through material of fixed thickness. The distribution can be written as

$$f(x, \Delta E) = \frac{1}{\xi}\varphi(\lambda). \tag{2.6}$$

ξ has form

$$\xi = d\frac{2\pi N_A e^4 \rho < Z/A >}{mc^2\beta}, \tag{2.7}$$

where ρ is material density and

$$\lambda = \frac{\Delta E - \Delta E_{MPV}}{\xi}. \tag{2.8}$$

ΔE_{MPF} is the most probable lost energy and can be expressed using analytical formula

$$\Delta E_{MPV} = \frac{Cd}{\beta^2}\left[ln\left(\frac{2Cm_e c^2 d\beta^2}{I^2(1-\beta^2)}\right) + 0.02 - \beta^2\right] \tag{2.9}$$

where

$$C = \frac{2\pi N_A z^2 e^4 \rho < Z/A >}{m_e c^2}\left(\frac{e^2}{4\pi\varepsilon_0}\right)^2. \tag{2.10}$$

Formula (2.9) could potentially be used as the new correction function. Compared to Bethe-Bloch formula there is no need for approximations or numerical solution which is a clear advantage. The Landau distribution has, however, also been derived using certain assumptions. Namely, it considers that the total energy of the particle is much higher than the energy which it losses. Such approximation might not be appropriate for our electrons of 482 keV.

Formulas described in this section could provide a basis for improved energy loss correction. Compared to purely empirical correction (2.2) these formulas contain parameters representing physical quantities dependent on properties of the detector. Because of that, parameters of model based on these formulas could be verified by comparison with their real values. It will be important to investigate how well models based on equations (2.3) and (2.9) describe the previously used simulated data and most importantly the real data. Such analysis will be the point of future study.

Summary

The goal of this thesis is to compare real data newly obtained by SuperNEMO detector with previously performed simulations. The first chapter contains brief introduction into neutrino physics, different experiments searching for $0\nu\beta\beta$-decay and the SuperNEMO experiment. The second chapter then focuses on data processing and comparisons.

The beginning of second chapter is focused on structure of SuperNEMO data. It describes raw signals obtained by the detector and different data formats used to store and analyze the data. Then different algorithms used for selection of events containing an electron emitted from a calibration source are described. It is shown that selection algorithm based on 3D track reconstruction is the most precise one. This algorithm is used to extract information from the real data. The work focuses on exposure of individual optical modules and the shape of measured spectra. The exposures are comparable with values obtained from the real data, although there are some differences which are probably caused by the fact that the selection algorithm used on the real data is not identical to the one which was used for simulations. In comparison of spectra shapes some differences has been found as well. The shape of the first peak seems to be different from the simulated data. This effect, however, is probably caused by current settings of the detector and will not be present in future data. Second difference is in the ratio of the peaks in the spectra. In simulated data the ratio is higher. In the thesis it is shown that application of the optical correction partially solves this discrepancy. In the last part of the thesis energy losses of electrons are discussed. These losses can significantly influence the precision of the calibration which is why it is important to describe them. Previously energy loss correction has been developed based on simulated data. This correction, however, has some flaws - it is purely empirical, it has too many fitting parameters and it does not seem to properly describe data which were newly simulated with settings more authentic to the real data. Finally, two different approaches, which could be used to create new energy loss model, are proposed. The first one is based on Bethe-Bloch formula and leads to an integral which cannot be solved analytically. A numerical or approximate solution is needed. The second approach is based on the Landau distribution. Its most probable value can be expressed by an analytical formula and could offer simpler way to develop new energy loss correction.

Bibliography

1. FUKUDA, Y. et al. Evidence for Oscillation of Atmospheric Neutrinos. *Physical Review Letters*. 1998, vol. 81, pp. 1562–1567. Available from DOI: 10.1103/PhysRevLett.81.1562.
2. LIPARI, P. Introduction to neutrino physics. In: *1st CERN-CLAF School of High-Energy Physics*. 2001, pp. 115–199.
3. CAHN, R. N. et al. *White Paper: Measuring the Neutrino Mass Hierarchy*. 2013. Available from arXiv: 1307.5487 [hep-ex].
4. AKER, M. et al. Improved Upper Limit on the Neutrino Mass from a Direct Kinematic Method by KATRIN. *Physical Review Letters*. 2019, vol. 123, no. 22, p. 221802. Available from DOI: 10.1103/physrevlett.123.221802.
5. AGHANIM, N. et al. Planck 2018 results: VI. Cosmological parameters. *Astronomy & Astrophysics*. 2020, vol. 641. Available from DOI: 10.1051/0004-6361/201833910.
6. KOŇAŘÍK, F. *Vývoj softwaru pro energetickou kalibraci pro SuperNEMO detektor*. 2022. Available also from: http://hdl.handle.net/10467/104011. Theses. FNSPE CTU in Prague.
7. GOEPPERT-MAYER, M. Double Beta-Disintegration. *Physical Review*. 1935, vol. 48, pp. 512–516. Available from DOI: 10.1103/PhysRev.48.512.
8. VOLKMER, J. *Prospects of the Iinvestigation of EC/Beta+ Decays With the COBRA Experiment*. 2018. MA thesis.
9. FURRY, W. H. On Transition Probabilities in Double Beta-Disintegration. *Physical Review*. 1939, vol. 56, pp. 1184–1193. Available from DOI: 10.1103/PhysRev.56.1184.
10. MACKO, M. *SuperNEMO Experiment : Study of Systematic Uncertainties of Track Reconstruction and Energy Calibration. Evaluation of Sensitivity to 0nbb with Emission of Majoron for Se-82*. 2018. Available also from: https://tel.archives-ouvertes.fr/tel-02122290. Theses. Université de Bordeaux ; Univerzita Komenského (Bratislava). Faculté de mathématiques, physique et informatique.
11. ACKERMANN, K.-H. et al. The Gerda experiment for the search of $0\nu\beta\beta$ decay in ^{76}Ge. *The European Physical Journal C*. 2013, vol. 73, no. 3. Available from DOI: 10.1140/epjc/s10052-013-2330-0.
12. GUISEPPE, V.E. et al. The MAJORANA neutrinoless double-beta decay experiment. In: 2008, pp. 1793–1798. Available from DOI: 10.1109/NSSMIC.2008.4774740.

13. GANDO, Y. et al. The nylon balloon for xenon loaded liquid scintillator in KamLAND-Zen 800 neutrinoless double-beta decay search experiment. *Journal of Instrumentation*. 2021, vol. 16, no. 08, P08023. Available from DOI: 10.1088/1748-0221/16/08/p08023.

14. GRATTA, G.; SINCLAIR, D. Present Status and Future Perspectives for the EXO-200 Experiment. *Advances in High Energy Physics*. 2013, vol. 2013, pp. 1–7. Available from DOI: 10.1155/2013/545431.

15. POCAR, Andrea; COLLABORATION, on behalf of the nEXO. The nEXO detector: design overview. *Journal of Physics: Conference Series*. 2020, vol. 1468, no. 1, p. 012131. Available from DOI: 10.1088/1742-6596/1468/1/012131.

16. FUJIKAWA, B.; LIGI, C. Search for Majorana neutrinos exploiting millikelvin cryogenics with CUORE. *Nature*. 2022, vol. 604, pp. 53–58. Available from DOI: 10.1038/s41586-022-04497-4.

17. ARNOLD, R. et al. Technical design and performance of the NEMO 3 detector. *Nuclear Instruments and Methods in Physics Research Section A: Accelerators, Spectrometers, Detectors and Associated Equipment*. 2005, vol. 536, no. 1, pp. 79–122. ISSN 0168-9002. Available from DOI: https://doi.org/10.1016/j.nima.2004.07.194.

18. BARABASH, A.S. et al. Calorimeter development for the SuperNEMO double beta decay experiment. *Nuclear Instruments and Methods in Physics Research Section A: Accelerators, Spectrometers, Detectors and Associated Equipment*. 2017, vol. 868, pp. 98–108. ISSN 0168-9002. Available from DOI: https://doi.org/10.1016/j.nima.2017.06.044.

19. ARNOLD, R. et al. Measurement of the distribution of ^{207}Bi depositions on calibration sources for SuperNEMO. *Journal of Instrumentation*. 2021, vol. 16, no. 07, T07012. Available from DOI: 10.1088/1748-0221/16/07/t07012.

20. HODÁK, R. et al. Improvement of the energy resolution of the scintillating detectors for the low background measurement. *AIP Conference Proceedings*. 2015, vol. 1672, no. 1, p. 130003. Available from DOI: 10.1063/1.4928013.

21. COLLABORATION, SuperNEMO. *Falaise documentation* [online] [visited on 2022-04-21]. Available from: https://supernemo.org/Falaise/index.html.

22. CERN. *GEANT4: A simulation toolkit* [online] [visited on 2022-05-01]. Available from: https://geant4.web.cern.ch/.

23. KŘIŽÁK, T. *TKEvent* [online] [visited on 2023-05-12]. Available from: https://github.com/TomasKrizak/TKEvent.

24. KŘIŽÁK, T. *Development of an algorithm for linear particle track reconstruction in SuperNEMO detector*. 2023. Available also from: http://hdl.handle.net/10467/111453. Theses. FNSPE CTU in Prague.

25. HUBER, Arnaud. *Recherche de la nature du neutrino avec le détecteur SuperNEMO : simulations optiques pour l'optimisation du calorimètre et performances attendues pour le 82Se*. 2017. Available also from: https://theses.hal.science/tel-01628463. Theses. Université de Bordeaux.

26. PIN, Axel. *Recherche de la nature du neutrino via la décroissance double bêta sans émission de neutrinos : Caractérisation et optimisation du calorimètre SuperNEMO et impact sur la recherche de la décroissance du 82Se : Développement du premier prototype LiquidO*. 2020. Available also from: `https://theses.hal.science/tel-03149593`. Theses. Université de Bordeaux.

27. BIRKS, J B. Scintillations from Organic Crystals: Specific Fluorescence and Relative Response to Different Radiations. *Proceedings of the Physical Society. Section A*. 1951, vol. 64, no. 10, p. 874. Available from DOI: `10.1088/0370-1298/64/10/303`.

28. BETHE, H.; ASHKIN, J. Passage of Radiations through Matter. *Experimental Nuclear Physics*. 1953, p. 253. Available also from: `https://hdl.handle.net/2027/mdp.39015003445122`.